Measurement of turbulence spectra using scanning pulsed wind lidars

Sathe, Ameya; Mann, Jakob

Published in:
Journal of Geophysical Research

Link to article, DOI:
10.1029/2011JD016786

Publication date:
2012

Measurement of turbulence spectra using scanning pulsed wind lidars

A. Sathe[1,2], J. Mann[1]

A. Sathe, Wind Energy Division, Risø DTU, Frederiksborgvej 399, 4000 Roskilde, Denmark. (amsat@risoe.dtu.dk)

J. Mann, Wind Energy Division, Risø DTU, Frederiksborgvej 399, 4000 Roskilde, Denmark.

[1]Wind Energy Division, Risø DTU,
Frederiksborgvej 399, 4000 Roskilde,
Denmark.

[2]Wind Energy Section, Faculty of
Aerospace Engineering, Delft University of
Technology, The Netherlands.

Abstract. Turbulent velocity spectra, as measured by a scanning pulsed wind lidar (WindCube), are analyzed. The relationship between ordinary velocity spectra and lidar derived spectra is mathematically very complex, and deployment of the three-dimensional spectral velocity tensor is necessary. The resulting scanning lidar spectra depend on beam angles, line-of-sight averaging, sampling rate, and the full three-dimensional structure of the turbulence being measured, in a convoluted way. The model captures the attenuation and redistribution of the spectral energy at high and low wavenumbers very well. The model and measured spectra are in good agreement at two analyzed heights for the u and w components of the velocity field. An interference phenomenon is observed, both in the model and the measurements, when the diameter of the scanning circle divided by the mean wind speed is a multiple of the time between the beam measurements. For the v spectrum, the model and the measurements agree well at both heights, except at very low wavenumbers, $k_1 < 0.005$ m^{-1}. In this region, where the spectral tensor model has not been verified, the model overestimates the spectral energy measured by the lidar. The theoretical understanding of the shape of turbulent velocity spectra measured by scanning pulsed wind lidar is given a firm foundation.

1. Introduction

This study aims to explain how a scanning pulsed wind lidar measures turbulence spectra in combination with the velocity azimuth display (VAD) technique of data processing. In particular, a theoretical model of the turbulence spectra measured by a pulsed wind lidar (WindCube) operating in a VAD mode is developed. The model is verified by comparing measurements from a lidar and a sonic anemometer (sonic).

Turbulence spectra are one of the main inputs in designing any physical structure where random variations in the atmosphere produce random vibrations in the structure, such as suspension bridges, tall buildings, and wind turbines. Wind turbines, in particular, are designed to withstand fatigue and extreme loads during their entire lifetime of approximately 20 years. For the turbulence spectra, the IEC standard [*IEC*, 2005] for wind turbine design prescribes either the Kaimal model [*Kaimal et al.*, 1972] or the more recent Mann model [*Mann*, 1994], which models the three-dimensional turbulent structure under neutral conditions. Besides normal variations of the wind field in the atmosphere, gusts are a major source of extreme loads on many civil engineering structures. Standard gust models can be used to characterize the input for these extreme loads, e.g., the gust models by *Davenport* [1964] and *Kristensen et al.* [1991] are derived from the so-called Rice theory [*Rice*, 1944, 1945], where the gust factor is proportional to the moments of turbulence spectra. Thus, the model of turbulence spectra in this study is also a prerequisite for obtaining a theoretical model of the gust factors measured by lidars.

In micrometeorology, the structure of turbulence consists of three well-defined regions: the energy containing range, inertial sub-range, and dissipative range [*Kaimal and Finni-*

gan, 1994]. Sonics are the current industry standard instrument to measure the first two turbulence regions that influence wind turbines and other structures. However, a meteorological mast (met-mast) is needed in order to support the boom-mounted sonics at several heights. This requirement leads to several disadvantages such as high installation costs for taller masts (particularly offshore), flow distortion due to the mast and booms, need for several instruments to cover all wind directions, and immobility of the mast. A ground-based remote sensing instrument such as a lidar provides an attractive alternative. In recent years, with the introduction of commercial wind lidars, there have been several verification campaigns for comparing the lidar mean wind speed with that of a cup anemometer for wind energy applications [*Courtney et al.*, 2008; *Peña et al.*, 2009]. Although the performance with respect to mean wind speed is currently relatively well understood, in order to use a lidar as a standard measuring instrument in the future, a fair degree of confidence is also required in the turbulence measurements.

Although new to wind energy, for meteorology, lidars have been investigated previously to measure turbulence using different scanning techniques. Turbulence statistics from lidars has actually been a topic of research since the 1960s. One of the early measurements of turbulence spectra was conducted by *Kunkel et al.* [1980], where only the longitudinal component of the wind field was measured in the convective boundary layer. Good comparisons were obtained with the spectral functions of *Kaimal et al.* [1976]. *Hardesty et al.* [1982] measured turbulence spectra in the surface layer by conically scanning lidar in the vertical plane. Large attenuations were observed in the mid-frequency range that were just below the scanning frequency, whereas additional spectral energy was observed at high frequencies because of the re-distribution of energy by sampling points rapidly in a circle.

A preliminary model was also constructed that explains the differences between the point and lidar spectra. *Mayor et al.* [1997] performed measurements of velocity spectra in the convective boundary layer using a staring lidar. Spatial averaging along the line-of-sight was modeled using a spectral transfer function, and an attempt was made to recover the true atmospheric spectra by observing inertial sub-range isotropy. *Frehlich et al.* [1998] investigated wind field statistics and turbulence spectra using lidars at different azimuth and half opening angles. *Drobinski et al.* [2000] measured turbulence spectra using a horizontally staring lidar beam, where spatial averaging in the line-of-sight velocity was modeled using the Kolmogorov spectrum. Good agreements between the modeled and measured spectra were obtained. The staring lidar configuration was also investigated by *Sjöholm et al.* [2009] and *Mann et al.* [2009] for measuring the turbulence spectra of line-of-sight velocities and modeling the corresponding transfer function, where the model agreed well with the measurements. *Lothon et al.* [2009] conducted a comprehensive study of vertical velocity spectra in the convective boundary layer, also using a vertically staring lidar. Different cases were found to sporadically agree with the *Kristensen et al.* [1989] spectral tensor model. However, because of large variability within different cases, a universal model of the vertical velocity spectra in the convective boundary layer could not be developed. *Canadillas et al.* [2010] compared turbulence spectra measured by a WindCube operating in a VAD mode with those measured by a sonic, and observed an unexplained increase in the energy between the energy containing range and the inertial sub-range. A sudden drop in energy was also observed in the inertial sub-range. *Dors et al.* [2011] performed turbulence spectra measurements in the Kelvin-Helmholtz layer by using a fixed lidar beam configuration and a thermosonde. The lidar measurements of the

turbulent kinetic energy dissipation rate agreed well with those from a thermosonde when the turbulence levels were high. Recently, *Sathe et al.* [2011] investigated the potential of lidars operating in a VAD mode to measure turbulence statistics, where it was concluded that large systematic errors are introduced in the measurement of second-order statistics of the wind field.

In the remaining sections, we concentrate on investigating how turbulence spectra are measured by a pulsed lidar. In section 2, we explain the basics of the WindCube measurements. The modeling of turbulence spectra is described in section 3. Some background of the measurements and the site is presented in section 4. Section 5 compares the model and the measurements at two heights. Finally, we draw conclusions from our study in section 6.

2. Lidar Measurement Basics

Fig. 1 shows the lidar emitting a laser beam at four azimuth angles, viz. North (N), East (E), South (S), and West (W). The line-of-sight velocity (also called radial velocity v_r) is measured by the lidar at respective azimuth angles. The half-opening angle ϕ ($= 90° -$ elevation angle) is maintained constant throughout the scan. In this study, the instrument has $\phi = 27.5°$. Wind lidars work on the principle of backscattering of the emitted radiation from suspended aerosols and subsequent detection of the Doppler shift in the frequency of the received radiation. The Doppler shift in the frequency is related to v_r, as given by

$$\delta f = 2\frac{v_r}{\lambda}, \tag{1}$$

where f and λ are the frequency and wavelength of the emitted radiation, respectively. Mathematically, measurement of the line-of-sight velocity by a scanning lidar is given as

the dot product of the unit vector in the direction of the measurement and the velocity field at the center of the measuring volume,

$$v_r(\theta) = \boldsymbol{n}(\theta) \cdot \mathbf{v}(d_f \boldsymbol{n}(\theta)), \tag{2}$$

where θ is the azimuth angle, d_f is the center of the range gate at which the wind speeds are measured, $\boldsymbol{n}(\theta) = (\cos\theta \sin\phi, \sin\theta \sin\phi, \cos\phi)$ is the unit directional vector, and $\mathbf{v} = (u, v, w)$ is the instantaneous velocity field evaluated at the range gate $d_f \boldsymbol{n}(\theta)$. In practice, for a lidar it is impossible to obtain the backscattered radiation precisely from a single point, and there is always backscattered radiation of different intensities from different regions in space along the line-of-sight. Hence, it is necessary to assign appropriate weights to the backscattered intensity such that the weight corresponding to the center of the range gate is the highest. For a pulsed lidar, a triangular weighting function $\varphi(s)$ is commonly assumed [*Lindelöw*, 2007], which is given as

$$\varphi(s) = \begin{cases} \frac{l_p - |s|}{l_p^2} & \text{for } |s| < l_p; \\ 0 & \text{elsewhere,} \end{cases} \tag{3}$$

where l_p is the half length of the ideally rectangular light pulse leaving the lidar, assuming matching time windowing ($= 2l_p/c$, where c is the speed of light). The weighted average radial velocity can thus be written as

$$\tilde{v}_r(\theta) = \int_{-\infty}^{\infty} \varphi(s)\ \boldsymbol{n}(\theta) \cdot \mathbf{v}(\boldsymbol{n}(\theta)(s + d_f))\ ds, \tag{4}$$

where s is the distance along the beam from the center of the range gate.

In this study, we derive expressions of turbulence spectra assuming that the wind comes from the North. The equations become too cumbersome if an arbitrary wind direction is considered. Nevertheless, the same framework can be used in modeling turbulence spectra

for any wind direction. Let us denote the unit vectors in the four directions as

$$\boldsymbol{n}_N = \boldsymbol{n}(-\Theta),\ \boldsymbol{n}_S = \boldsymbol{n}(\pi - \Theta),\ \boldsymbol{n}_E = \boldsymbol{n}(\frac{\pi}{2} - \Theta),\ \boldsymbol{n}_W = \boldsymbol{n}(3\frac{\pi}{2} - \Theta), \tag{5}$$

where the subscripts of the unit vectors indicate respective directions and Θ is the wind direction. In this study, we use $\Theta = 0$. If we consider the coordinate system such that the u component is aligned in the mean wind direction, then from simple geometrical considerations for $\Theta = 0$, we get

$$\begin{aligned} u_{wc} &= \frac{\tilde{v}_{rS} - \tilde{v}_{rN}}{2\sin\phi}, \\ v_{wc} &= \frac{\tilde{v}_{rE} - \tilde{v}_{rW}}{2\sin\phi}, \end{aligned} \tag{6}$$

where the subscript wc denotes the measurement by the WindCube, and $\tilde{v}_{rN}$, $\tilde{v}_{rS}$, $\tilde{v}_{rE}$, and $\tilde{v}_{rW}$ are the weighted average radial velocities in the North, South, East, and West directions, respectively. For the w component, we use the formula by the company that produces the WindCube, Leosphere,

$$w_{wc} = \frac{P(\tilde{v}_{rN} + \tilde{v}_{rS}) + Q(\tilde{v}_{rE} + \tilde{v}_{rW})}{2\cos\phi}, \tag{7}$$

where P and Q are the weights associated with the wind direction such that $P + Q = 1$. Leosphere uses $P = \cos^2\Theta$ and $Q = \sin^2\Theta$, and hence, we use the same in our calculations. Thus, for $\Theta = 0$ we get

$$w_{wc} = \frac{\tilde{v}_{rN} + \tilde{v}_{rS}}{2\cos\phi}. \tag{8}$$

Further details of the working principles of the WindCube are given in *Lindelöw* [2007].

3. Modeling the turbulence spectra measured by a pulsed wind lidar

By definition, the one-dimensional spectrum of any component of the wind field is given as [*Wyngaard*, 2010]

$$\begin{aligned} F_{ij}(k_1) &= \frac{1}{2\pi}\int_{-\infty}^{\infty} R_{ij}(x)\exp(-\mathrm{i}k_1 x)\ dx, \\ &= \frac{1}{2\pi}\lim_{X\to\infty}\int_{-X}^{X} R_{ij}(x)\exp(-\mathrm{i}k_1 x)\left(\frac{1-|x|}{X}\right)\ dx, \end{aligned} \tag{9}$$

where k_1 is the wavenumber, $F_{ij}(k_1)$ is the one-dimensional spectrum, $R_{ij}(x)$ is the auto-covariance function, x is the separation distance, and X is the length of the record. Since the WindCube cannot make continuous measurements, let us take only discrete values such that $X = N\Delta x$ and $x = n\Delta x$, where n is an integer multiple, N is the total number of samples, and Δx is the distance traveled by the wind when the lidar beam shifts from one azimuth angle to the other. Since it takes about 4 s for the WindCube beam to move from the North to the South, or from the East to the West, assuming Taylor's hypothesis to be valid, we get $\Delta x = \bar{u} \times 4$ m, where $\bar{u}$ is the mean wind speed. If we evaluate the spectra measured by the WindCube at only discrete wave numbers $k_{1_q} = 2\pi q/X$, then we can write

$$F_{ij_{wc}}(q) = \frac{1}{2\pi}\sum_{n=-N}^{N} R_{ij_{wc}}(n)\exp\left(\frac{-\mathrm{i}2\pi nq}{N}\right)\left(1-\frac{|n|}{N}\right)\ \Delta x. \tag{10}$$

The challenge now is to find an expression for $R_{ij_{wc}}(n)$. As in *Sathe et al.* [2011], we make the following assumptions:

1. The flow is horizontally homogeneous and Taylor's hypothesis is valid.

2. The spatial structure of the turbulent flow is described well by the spectral tensor model of *Mann* [1994].

We first demonstrate the model of $R_{ij_{wc}}(n)$ for the u component and use the same framework to derive the v and w components.

We begin by considering the mathematical form of Taylor's hypothesis such that

$$\mathbf{v}(x,t) = \mathbf{v}(x - \Delta x, 0), \tag{11}$$

where t is the time. For simplicity, let us first neglect the averaging along the line-of-sight. We will introduce this averaging later in the equations. For the turbulence spectra measured by the WindCube, it is necessary to consider the exact spatial and temporal position of the measurements. The wind vector is constructed using the North and South beams such that at any given instant, one current and one previous measurement is used. If we assume that at $t = 0$, we use the current measurement from the North beam and the previous measurement from the South beam, then combining Eqs. (6) and (11) we can write

$$u_{wc}(m\Delta x) = \frac{\tilde{v}_{rS}(\boldsymbol{n}_S d_f - \boldsymbol{e}_1(m-1)\Delta x) - \tilde{v}_{rN}(\boldsymbol{n}_N d_f - \boldsymbol{e}_1 m\Delta x)}{2\sin\phi}, \text{ for even } m, \tag{12}$$

$$u_{wc}(m\Delta x) = \frac{\tilde{v}_{rS}(\boldsymbol{n}_S d_f - \boldsymbol{e}_1 m\Delta x) - \tilde{v}_{rN}(\boldsymbol{n}_N d_f - \boldsymbol{e}_1(m-1)\Delta x)}{2\sin\phi}, \text{ for odd } m, \tag{13}$$

where $\boldsymbol{e}_1 = (1,0,0)$ is the unit vector in the mean wind direction. Combining even and odd m from Eqs. (12) and (13), we can write

$$\begin{aligned} u_{wc}(m\Delta x) = &\Big[\tilde{v}_{rS}\Big(\boldsymbol{n}_S d_f - \boldsymbol{e}_1\big(m - \frac{(1+(-1)^m)}{2}\big)\Delta x\Big) \\ &- \tilde{v}_{rN}\Big(\boldsymbol{n}_N d_f - \boldsymbol{e}_1\big(m - \frac{(1-(-1)^m)}{2}\big)\Delta x\Big)\Big] \Big/ \Big(2\sin\phi\Big). \end{aligned} \tag{14}$$

We know that by definition, $R_{ij}(n) = \langle u_i(m\Delta x) u_j\big((m+n)\Delta x\big)\rangle$, where $\langle\rangle$ denotes ensemble averaging. By applying this definition to Eq. (14), we get auto and cross covariances for the North and South beams. Introducing the averaging along the beam (using Eq. 4)

for only the south beam, we get

$$\Big\langle \tilde{v}_{rS}\Big(\boldsymbol{n}_S d_f - \boldsymbol{e}_1\big(m - \frac{(1+(-1)^m)}{2}\big)\Delta x\Big)\tilde{v}_{rS}\Big(\boldsymbol{n}_S d_f - \boldsymbol{e}_1\big((m+n) - \frac{(1+(-1)^{m+n})}{2}\big)\Delta x\Big)\Big\rangle$$
$$= \int_{-\infty}^{\infty}\int_{-\infty}^{\infty} n_{iS}n_{jS}\ \varphi(s_1)\varphi(s_2)$$
$$\Big\langle \mathrm{v}_i\Big(\boldsymbol{n}_S d_f - \boldsymbol{e}_1\big(m - \frac{(1+(-1)^m)}{2}\big)\Delta x + \boldsymbol{n}_S s_1\Big)$$
$$\mathrm{v}_j\Big(\boldsymbol{n}_S d_f - \boldsymbol{e}_1\big((m+n) - \frac{(1+(-1)^{m+n})}{2}\big)\Delta x + \boldsymbol{n}_S s_2\Big)\Big\rangle\ ds_1 ds_2 \tag{15}$$

If we denote $\boldsymbol{r} = \Big(\boldsymbol{n}_S d_f - \boldsymbol{e}_1\big(m - (1+(-1)^m)/2\big)\Delta x\Big) - \Big(\boldsymbol{n}_S d_f - \boldsymbol{e}_1\big((m+n) - (1+(-1)^{m+n})/2\big)\Delta x\Big)$ as the separation distance between the S-S beam combination, then we can write

$$R_{\tilde{v}_{rS}}(n) = \int_{-\infty}^{\infty}\int_{-\infty}^{\infty} n_{iS}n_{jS}\ \varphi(s_1)\varphi(s_2)R_{ij}(\boldsymbol{r} + \boldsymbol{n}_S(s_1 - s_2))\ ds_1 ds_2, \tag{16}$$

where $R_{\tilde{v}_{rS}}(n)$ is the autocovariance of the radial velocity for the South beam. $R_{ij}(\boldsymbol{r})$ is related to the three dimensional spectral velocity tensor $\Phi_{ij}(\boldsymbol{k})$ by the inverse Fourier transform [*Wyngaard*, 2010], i.e.,

$$R_{ij}(\boldsymbol{r} + \boldsymbol{n}_S(s_1 - s_2)) = \int \Phi_{ij}(\boldsymbol{k})\exp(\mathrm{i}\boldsymbol{k}\cdot(\boldsymbol{r} + \boldsymbol{n}_S(s_1 - s_2)))\ d\boldsymbol{k}, \tag{17}$$

where $\int d\boldsymbol{k} \equiv \int_{-\infty}^{\infty}\int_{-\infty}^{\infty}\int_{-\infty}^{\infty} dk_1 dk_2 dk_3$ and $\boldsymbol{k} = (k_1, k_2, k_3)$ denotes the wave vector. Substituting Eq. (17) into (16) and rearranging the terms, we get

$$R_{\tilde{v}_{rS}}(\boldsymbol{r}) = \int \Phi_{ij}(\boldsymbol{k})\ n_{iS}n_{jS}\ \exp(\mathrm{i}\boldsymbol{k}\cdot\boldsymbol{r})\ \hat{\varphi}(\boldsymbol{k}\cdot\boldsymbol{n}_S)\hat{\varphi}^*(\boldsymbol{k}\cdot\boldsymbol{n}_S)\ d\boldsymbol{k} \tag{18}$$

where $\hat{}$ denotes Fourier transform and * complex conjugation. Reducing the expression of $\boldsymbol{r}$, we get

$$\boldsymbol{r} = \boldsymbol{e}_1\Big((-1)^m\frac{\Delta x}{2}(1-(-1)^n) + n\Delta x\Big). \tag{19}$$

Similarly, if we assume that at $t = 0$ we use the current measurement from the South beam and the previous measurement from the North beam, then we get

$$\begin{aligned} u_{wc}(m\Delta x) = &\Big[\tilde{v}_{rS}\Big(\boldsymbol{n}_S d_f - \boldsymbol{e}_1\big(m - \frac{(1-(-1)^m)}{2}\big)\Delta x\Big) \\ &- \tilde{v}_{rN}\Big(\boldsymbol{n}_N d_f - \boldsymbol{e}_1\big(m - \frac{(1+(-1)^m)}{2}\big)\Delta x\Big)\Big] \Big/ \Big(2\sin\phi\Big), \end{aligned} \tag{20}$$

and the separation distance for the S-S beam combination is given as $\boldsymbol{r} = -(-1)^m \Delta x/2(1-(-1)^n) + n\Delta x$. In order to make the time series statistically stationary, we consider that there is an equal probability that the beam at $t = 0$ points either in the North or South direction. This eliminates the dependence of the autocovariance function on m. We perform similar analysis on the auto and cross covariances for other beams. In total, we then get eight separation distances; two for the S-S, two for S-N, two for N-S, and two for N-N beam combinations. If we denote $\boldsymbol{r}_{u_l}$ (the subscript l denotes the respective beam combination) as the separation distance for different beam combinations, then we can write all the separation distances in compact form as

$$\boldsymbol{r}_{u_l} = \begin{cases} \boldsymbol{e}_1\Big((-1)^l \frac{\Delta x}{2}(1-(-1)^n) + n\Delta x\Big) & \text{for } l = 1,2,7,8; \\ \boldsymbol{n}_S d_f - \boldsymbol{n}_N d_f + \boldsymbol{e}_1\Big((-1)^l \frac{\Delta x}{2}(1+(-1)^n) + n\Delta x\Big) & \text{for } l = 3,4; \\ \boldsymbol{n}_N d_f - \boldsymbol{n}_S d_f + \boldsymbol{e}_1\Big((-1)^l \frac{\Delta x}{2}(1+(-1)^n) + n\Delta x\Big) & \text{for } l = 5,6. \end{cases} \tag{21}$$

Following a similar procedure for the v component, we get the following separation distances:

$$\boldsymbol{r}_{v_l} = \begin{cases} \boldsymbol{e}_1\Big((-1)^l \frac{\Delta x}{2}(1-(-1)^n) + n\Delta x\Big) & \text{for } l = 1,2,7,8; \\ \boldsymbol{n}_E d_f - \boldsymbol{n}_W d_f + \boldsymbol{e}_1\Big((-1)^l \frac{\Delta x}{2}(1+(-1)^n) + n\Delta x\Big) & \text{for } l = 3,4; \\ \boldsymbol{n}_W d_f - \boldsymbol{n}_E d_f + \boldsymbol{e}_1\Big((-1)^l \frac{\Delta x}{2}(1+(-1)^n) + n\Delta x\Big) & \text{for } l = 5,6. \end{cases} \tag{22}$$

The separation distances for the w component are the same as those for the u component, because only the North and South beams are used to obtain w_{wc} (Eq. 8). Combining Eqs. (12)–(22) and using the symmetry properties of $\Phi_{ij}(\boldsymbol{k})$, we get the expressions for

the autocovariance of the u and v components as

$$R_{u_{wc}}(n) = \frac{1}{8\sin^2\phi}\int \Phi_{ij}(\boldsymbol{k})\Big[n_{iS}n_{jS}\hat{\varphi}(\boldsymbol{k}\cdot\boldsymbol{n}_S)\hat{\varphi}^*(\boldsymbol{k}\cdot\boldsymbol{n}_S)\sum_{l=1}^{2}\exp(\mathrm{i}\boldsymbol{k}\cdot\boldsymbol{r}_{u_l}) - n_{iS}n_{jN}\hat{\varphi}(\boldsymbol{k}\cdot\boldsymbol{n}_S)\hat{\varphi}^*(\boldsymbol{k}\cdot\boldsymbol{n}_N)\sum_{l=3}^{6}\exp(\mathrm{i}\boldsymbol{k}\cdot\boldsymbol{r}_{u_l}) + n_{iN}n_{jN}\hat{\varphi}(\boldsymbol{k}\cdot\boldsymbol{n}_N)\hat{\varphi}^*(\boldsymbol{k}\cdot\boldsymbol{n}_N)\sum_{l=7}^{8}\exp(\mathrm{i}\boldsymbol{k}\cdot\boldsymbol{r}_{u_l})\Big]d\boldsymbol{k}, \tag{23}$$

$$R_{v_{wc}}(n) = \frac{1}{8\sin^2\phi}\int \Phi_{ij}(\boldsymbol{k})\Big[n_{iE}n_{jE}\hat{\varphi}(\boldsymbol{k}\cdot\boldsymbol{n}_E)\hat{\varphi}^*(\boldsymbol{k}\cdot\boldsymbol{n}_E)\sum_{l=1}^{2}\exp(\mathrm{i}\boldsymbol{k}\cdot\boldsymbol{r}_{v_l}) - n_{iE}n_{jW}\hat{\varphi}(\boldsymbol{k}\cdot\boldsymbol{n}_E)\hat{\varphi}^*(\boldsymbol{k}\cdot\boldsymbol{n}_W)\sum_{l=3}^{6}\exp(\mathrm{i}\boldsymbol{k}\cdot\boldsymbol{r}_{v_l}) + n_{iW}n_{jW}\hat{\varphi}(\boldsymbol{k}\cdot\boldsymbol{n}_W)\hat{\varphi}^*(\boldsymbol{k}\cdot\boldsymbol{n}_W)\sum_{l=7}^{8}\exp(\mathrm{i}\boldsymbol{k}\cdot\boldsymbol{r}_{v_l})\Big]d\boldsymbol{k}. \tag{24}$$

The expression for the w component is similar to that for the u component, except that the second term in the square brackets of Eq. (23) is added instead of subtracted, and $\sin^2\phi$ is replaced by $\cos^2\phi$ in the denominator. Substituting Eqs. (23) and (24) into Eq. (10), we can finally theoretically calculate the turbulence spectra measured by the WindCube for the u, v, and w components of the velocity field.

In order to see the extent of attenuation and redistribution of the spectral energy, we compare these models with the true theoretical spectra measured by sonics and those measured by the WindCube. The true theoretical spectrum of any component of the wind field is also given as (apart from Eq. 9) [*Wyngaard*, 2010],

$$F_{ij}(k_1) = \int_{-\infty}^{\infty}\int_{-\infty}^{\infty}\Phi_{ij}(\boldsymbol{k})\; dk_2 dk_3. \tag{25}$$

We consider the sonic measurements to essentially represent the true theoretical spectra.

4. Description of the measurements

The measurements were performed at the Danish National Test Center for Large Wind Turbines at Høvsøre, Denmark. A reference met-mast, which is 116.5 m tall and intensively equipped with cup and sonic anemometers, is located at the coordinates 56°26'26" N, 08°09'03" E. The site is about 2 km from the West coast of Denmark. The eastern sector is generally characterized by a flat, homogeneous terrain, and to the South is a lagoon. To the North, there is a row of five wind turbines. The sonics are placed on the North booms of the met-mast, resulting in unusable data when the wind is from the south because of the wake of the mast, and from the North because of the wakes of the wind turbines.

We use the Metek USA-1 sonic measurements at 60 and 100 m in combination with the WindCube ($\approx$ 30 m range resolution) to compare with the modeled turbulence spectra. The WindCube is located about 5 m North-West of the met-mast, and the data were collected between January and April 2009. In order to avoid interference with the met-mast, the WindCube is turned in a horizontal plane such that the nominal North beam is 45° (i.e., in a North-East direction) with respect to true North. The frequency of measurement for the sonics is 20 Hz, whereas the WindCube takes approximately 2 s to shift from one azimuth angle to the other. We use the measurements from a narrow directional sector of 130°–140° only in order to align the mean wind direction with the nominal E-W beam of the WindCube. Thus, the u and w component measurements are deduced from the nominal E-W beams and the v component measurements are deduced from the nominal N-S beams. In order to avoid further confusion with Eqs. (6) and (8), the nominal E-W beam in the measurement is essentially the N-S beam in the theory, and vice-versa.

The other criteria for the selection of the data are neutral atmospheric stability and a mean wind speed of 9 m/s. This wind speed was chosen because the *Mann* [1994] model parameters were available at 9 m/s. Using Taylor's hypothesis, we then have the sampling distance in the mean wind direction $\Delta x = 9 \times 4$ m. We selected the data with a mean wind speed in the interval 8-10 m/s, which resulted in 79 and 58 10-min time series of the sonics and the WindCube at 60 and 100 m, respectively. Atmospheric stability is characterized using the standard surface-layer length scale L_{MO}, commonly known as the Monin-Obukhov length. Following *Gryning et al.* [2007], the conditions are considered neutral when $|L_{MO}| > 500$. L_{MO} is estimated using the eddy covariance method [*Kaimal and Finnigan*, 1994] from the sonic measurements at 20 m. Mathematically, L_{MO} is given as

$$L_{MO} = -\frac{{u_*}^3 T}{\kappa g \overline{w'\theta'_v}}, \tag{26}$$

where u_* is the friction velocity, $\kappa = 0.4$ is the von Kármán constant, g is the acceleration due to gravity, T is the absolute temperature, θ_v is the virtual potential temperature, and $\overline{w'\theta'_v}$ (covariance of w and θ_v) is the virtual kinematic heat flux. u_* is estimated as

$$u_* = \sqrt[4]{\overline{u'w'}^2 + \overline{v'w'}^2}, \tag{27}$$

where $\overline{u'w'}$ and $\overline{v'w'}$ are the vertical fluxes of the horizontal momentum.

The precision of the sonics is estimated to be about ±1.5%. Comparing with cup anemometers, the mean error of the WindCube in typical flat coastal conditions is within ±0.05 m/s, with a standard deviation in mixed shear conditions of about 0.15 m/s. A detailed list of different error sources is given by *Lindelöw-Marsden* [2009]. More details of the site and instrumentation can be found in *Sathe et al.* [2011].

5. Comparison of the model with the measurements

In order to calculate $\Phi_{ij}(\boldsymbol{k})$ in Eqs. (23)–(25), we use the model by *Mann* [1994]. It requires three model parameters, $\alpha\epsilon^{2/3}$, which is a product of the spectral Kolmogorov constant α [*Wyngaard*, 2010] and the rate of viscous dissipation of specific turbulent kinetic energy to the two-thirds power $\epsilon^{2/3}$, a length scale L and an anisotropy parameter Γ. In this study, these model parameters are obtained at 60 and 100 m by a χ^2-fit of the sonic measurements under neutral conditions (Eq. 4.1 from *Mann* [1994]) within the chosen directional sector of 130°–140°. As a result, the *Mann* [1994] model and the measurements agree very well for the sonics. The fitted model parameters are given in table 1. The *Mann* [1994] model is such that analytical expressions of $R_{ij}(\boldsymbol{r})$ and $F_{ij}(k_1)$ from $\Phi_{ij}(\boldsymbol{k})$ are not possible by integrating over the $\boldsymbol{k}$ domain. Hence, we use numerical integration based on adaptive algorithm [*Genz and Malik*, 1980] in order to calculate the integrals in Eqs. (23)–(25).

5.1. u spectrum

Fig. 2 shows the comparison of the modeled and measured u spectrum at 60 and 100 m. The measurements indicate that the spectrum measured by the WindCube deviates significantly from the standard surface-layer spectrum as the turbulence scales decrease approximately from $k_1 > 0.005$ m^{-1}. Approximately in the inertial sub-range, where the sonic spectra scales with $k_1^{-5/3}$, there is an almost complete attenuation of the turbulence signal, and hence a rapid decrease in the spectral energy. This observation has a striking resemblance with that of *Canadillas et al.* [2010], where an independent measurement under neutral conditions in the German North Sea showed an increase in the spectral energy above $k_1 > 0.005$ m^{-1} and subsequent rapid attenuation. One of the reasons for this

redistribution of the spectral energy is the contribution of the auto and cross covariances of different components of the velocity field, as seen in Eq. (23). At very low wavenumbers (< 0.005 m^{-1}), the spectral energy measured by the WindCube is approximately the same as that measured by the sonics. This is because very large turbulence eddies are associated with very low wavenumbers that cause the volume measurement from the lidar to behave essentially like a point measurement.

At both heights, our model agrees very well with the measurements at almost all wavenumbers. The point-like behavior of the WindCube at very low wavenumbers, and redistribution of the spectral energy beyond $k_1 > 0.005$ m^{-1}, is captured by the model very well. However, there are stark differences in the distribution of the spectral energy at 60 and 100 m. This is because of the beam interference phenomenon that occurs for certain separation distances at 100 m. This is explained as follows.

In our model, we have assumed validity of Taylor's hypothesis, which states that turbulence is advected by the mean wind field, i.e., the local velocity of the turbulent eddies is so small that they essentially move with only the mean velocity. In other words, turbulence can be considered to be frozen. For the u spectrum, we use only the N-S beams that are aligned in the mean wind direction. At 100 m, the mean wind speed is such that the North and South beams will investigate the same air (but different components) after approximately $3\Delta x$. Looking more closely at Eq. (21), at $3\Delta x$ we get $r_{u_3} \to 0$ and $r_{u_4} \to 0$. This implies that in Eq. (23), $\exp(\mathrm{i}\boldsymbol{k} \cdot r_{u_3}) \to 1$ and $\exp(\mathrm{i}\boldsymbol{k} \cdot r_{u_4}) \to 1$. This will cause an overall decrease in $R_{u_{wc}}(n)$ at $n = 3$. From our calculations, we also find anomalous behavior of $R_{u_{wc}}(n)$ at $n = 2$ and $n = 4$. Revisiting Eq. (21), we find that at $n = 2$, $r_{u_3} \to 0$ and at $n = 4$, $r_{u_4} \to 0$. This implies that it will cause some reduction in

198 $R_{u_{wc}}(n)$, but not as much as when $n = 3$. In order to explain this behavior, we illustrate
199 the interference phenomenon of the beams in Fig. 3.

Since we assume Taylor's hypothesis, we can either fix the N-S beams and measure the flow field as it moves past the beams, or freeze the flow field and move the N-S beams instead. For simplicity, let us freeze the flow field and represent 1–8 as the positions at which the North and the South beams perform measurements. The difference between each position is then equal to the separation distance Δx. Let 1, 3, 5, and 7 denote the measurements of the North beam and 2, 4, 6, and 8 denote those of the South beam. For now, let us consider only the intersection of beams 2 and 5 at point A, which is the point where the North and South beams will see the same air. This occurs at a separation distance of $3\Delta x$ corresponding to a height of 104 m. As a result, we will get unusual covariances whenever there is intersection of beams 2 and 5 in combination with other beam measurements. Since the WindCube uses one current and one previous measurement to deduce wind field components, we use the measurement from beam 2 when it is in combination with beam 1 or 3. Similarly, we use beam 5 when it is in combination with beam 4 or 6. These combinations can be written as

$$\begin{bmatrix} (\mathbf{2}, 1) & (\mathbf{3}, 2) \\ (\mathbf{5}, 4) & (\mathbf{6}, 5) \end{bmatrix} \tag{28}$$

200 The bold numbers in Eq. (28) indicate the current measurement for the respective beams,
201 i.e., the set $(\mathbf{2}, 1)$ indicates that the current measurement from beam 2 is used in combi-
202 nation with the previous measurement from beam 1 to deduce the u component, and so
203 on for other sets. In this case, we will obtain unusual covariances at these separation dis-
204 tances in the model, which are equal to the difference between beam numbers in bold (Eq.
205 28) that correspond to the intersection of beams 2 and 5. This happens at $\mathbf{5} - \mathbf{3}$, $\mathbf{5} - \mathbf{2}$,

and $\mathbf{6-2}$, corresponding to separation distances of $2\Delta x$, $3\Delta x$, and $4\Delta x$, respectively. We do not get unusual covariances at $\mathbf{3-2}$ because the sets $(\mathbf{2},1)$ and $(\mathbf{3},2)$ do not contain beam 5, and similarly at $\mathbf{6-5}$, since the sets $(\mathbf{5},4)$ and $(\mathbf{6},5)$ do not contain beam 2. Thus, in general, we will always obtain unusual covariances at the heights at which the distance between the North and the South beams corresponds to separation distances of $(n-1)\Delta x$, $n\Delta x$, and $(n+1)\Delta x$ (where n is odd, since for even n the North and South beams never intersect). Thus, if we now consider intersection points B ($\approx$ 35 m) and C ($\approx$ 173 m) in Fig. 3, then the separation distances are Δx and $5\Delta x$, respectively. Thus, we should expect unusual covariances at 0, Δx, and $2\Delta x$ at 35 m, whereas at 173 m, we expect the same at $4\Delta x$, $5\Delta x$, and $6\Delta x$.

In order to verify the above explanation, $R_{u_{wc}}(n)/\sigma_u^2$ (where σ_u^2 is the true variance of the u component) is calculated at two separation distances (100 and 173 m), as shown in Fig. 4. We do not calculate $R_{u_{wc}}(n)/\sigma_u^2$ at 35 m because the WindCube reliably measures from approximately 40 m (owing to a large measuring volume of about 30 m). σ_u^2 is calculated by integrating Eq. (25) over the k_1 domain at respective heights. We can now clearly see unusual covariances at $(n-1)\Delta x$, $n\Delta x$, and $(n+1)\Delta x$ at both heights, where $n = 3$ at 100 m and $n = 5$ at 173 m. Fig. 2 indicates that the model captures this beam interference phenomenon, which is also present in the measurements at 100 m, very well. Thus, it could also be implied that in nature, Taylor's hypothesis is valid to some extent.

5.2. v spectrum

Fig. 5 shows the comparison of the modeled and measured v spectrum at 60 and 100m. As observed for the u component, the v spectrum measured by the lidar deviates significantly from that of the sonic spectrum. However, at very low wavenumbers, there is

an offset in the spectral energy between the lidar and the sonic. The behavior in the inertial sub-range is the same as that for the u component, where a rapid attenuation in the spectral energy is observed. Our model agrees very well with the measurements at 60 and 100 m, except at very low wavenumbers (< 0.005 m^{-1}), where the model over estimates the spectral energy. One striking feature of this comparison is that as opposed to the u component, we do not see any beam interference phenomenon at 100 m because of Taylor's hypothesis. This is because only the E-W beams are used to deduce the v components, which are perpendicular to the mean wind field. Thus, even though we assume Taylor's hypothesis, the beams never interfere with each other at any separation distance. Thus, this result indirectly verifies the beam interference phenomenon explanation for the u component at 100 m. We give the following explanation for the over estimation of the spectral energy at very low wavenumbers.

From Eq. (24), it is understood that the v spectrum measured by the WindCube contains contributions from the v and w components of the spectral tensor, i.e., $\Phi_{22}(\boldsymbol{k})$ and $\Phi_{33}(\boldsymbol{k})$, weighted by the corresponding weighting functions $|\varphi(\boldsymbol{k}\cdot\boldsymbol{n}_E)|^2$ and $|\varphi(\boldsymbol{k}\cdot\boldsymbol{n}_W)|^2$. Due to the assumption of uniform shear and no effect of the Coriolis force by *Mann* [1994], the symmetry group of the spectral tensor model is such that the co-spectral energy between v and w is zero, i.e., $F_{23}(k_1) = 0$. We observed, using sonic anemometer measurements, that $F_{23}(k_1)$ is not exactly zero, but has some negative spectral energy at all wavenumbers. We also observed that $F_{23}(k_1) < F_{13}(k_1)$. On closely analyzing Eq. (24), we note that, in nature, if $F_{23}(k_1)$ contributes to the covariance measured by the lidar, it will result in overall reduction of $R_{v_{wc}}$. Thus, the symmetry group of *Mann* [1994] may not be entirely valid. We also find that the contribution of the second term in Eq. (24) is negligible,

and only the first and the third terms add to the spectral energy. Let us now consider a case such that at 60 m, the beam is staring perpendicularly to the mean wind field in a horizontal plane. It will thus measure only the v component of the velocity field. In this case, the v spectrum measured by the WindCube is given as

$$F_{v_{wc*}}(k_1) = \int_{-\infty}^{\infty} \Big(\int_{-\infty}^{\infty} \Phi_{22}(\boldsymbol{k})\, dk_3 \Big) |\hat{\varphi}(k_2)|^2\, dk_2, \tag{29}$$

where $*$ denotes spectra for a staring beam lidar. In Eq. (29), we first integrate over the k_3 domain, and the resulting two dimensional spectrum $E_v(k_1, k_2)$ is weighted by the filter function $|\hat{\varphi}(k_2)|^2$. The behavior of the weighting function is such that $|\hat{\varphi}(k_2)|^2 \to 1$ as $k_2 \to 0$. Thus, if the amount of two dimensional spectral energy increases sharply as $(k_1, k_2) \to 0$, then the contribution of this spectral energy in the one-dimensional spectrum will be significant. In order to verify this assumption, we calculate $E_v(k_1, k_2)$ at three values of k_1, i.e., $k_1 = (10^{-1}, 10^{-2}, 10^{-3})$ m^{-1}, as shown in Fig. 6. We also plot the variation of $|\hat{\varphi}(k_2)|^2$, so that filtering of the spectral energy for the respective wavenumbers is clearly evident. From the figure, it is observed that $k_1 \to 0$, $E_v(k_1, k_2)$ increases by several orders of magnitude with decreasing $|k_2|$ until a certain value of $|k_2|$, after which it decreases with $k_2 \to 0$. Since *Mann* [1994] does not assume isotropy in the horizontal plane, $E_v(k_1, k_2) \nrightarrow 0$ as $(k_1, k_2) \to 0$ [*Wyngaard*, 2010]. In our study, the WindCube is not horizontal, but at $\phi = 27.5°$ with the vertical. Hence, for the v component, the filter function along the line-of-sight acts over k_2 and k_3 domains. Its influence on averaging of the two and three dimensional spectral energy will be much more complicated than that for a horizontally pointing lidar. Nevertheless, we can argue similar reasons for the conically scanning case.

From the above explanation, we can consider four reasons for the over estimation of $F_{v_{wc}}(k_1)$ in the model as $k_1 \to 0$.

1. $E_v(k_1, k_2)$ could be more spread out such that the total energy over the k_2 domain would still be the same as that predicted by the *Mann* [1994] model.

2. The peak in $E_v(k_1, k_2)$ could be shifted to larger values of $|k_2|$.

3. Despite anisotropic conditions, $E_v(k_1, k_2)$ could approach zero as $(k_1, k_2) \to 0$.

4. There could be some contribution by $F_{23}(k_1)$.

As a consequence, the *Mann* [1994] model would still predict $F_v(k_1)$ considerably accurate. However, when $E_v(k_1, k_2)$ is weighted by $|\hat{\varphi}(k_2)|^2$, the total energy calculated using the *Mann* [1994] model and that obtained in nature would be different. Thus, it will cause overestimation of $F_{v_{wc}}(k_1)$ as $k_1 \to 0$, despite observing a good agreement between the theoretical and measured $F_v(k_1)$ (Fig. 5). Unfortunately, it is very difficult to measure the two- and three-dimensional spectra, and hence, we cannot verify our explanation.

5.3. *w* spectrum

Fig. 7 shows the comparison of the modeled and measured w spectrum at 60 and 100 m. Since in the calculation of the w spectrum, we use only the North and South beams, we will obtain similar beam interference at 100 m, because of the assumption of Taylor's hypothesis, as that observed for the u spectrum. The measured WindCube spectrum agrees quite well with the model at both heights, especially at high wavenumbers. As observed for the u component, at 100 m we note the effect of unusual covariances on the spectral energies. At very low wavenumbers, there is a slight offset between the model and measurements. This offset could be because of the slight deviation in the modeled and measured sonic spectrum. The model also shows that at very low wavenumbers, because

of very large turbulence eddies, the volume measurement from the lidar behaves similar to a point measurement.

6. Conclusion

The main objective of this paper is to understand how a pulsed wind lidar measures turbulence spectra. For this purpose, we modeled the u, v, and w spectra as measured by the WindCube only for a case where the mean wind direction is aligned with the measurement beams. For an arbitrary wind direction, a similar framework can be used, but it is much more complicated. In general, the model agrees very well with the measurements for all three components at both heights, except at very low wavenumbers for the v component.

For the u and w components at very low wavenumbers (< 0.005 m^{-1}), the volume measurement of the lidar behaves similar to a point measurement because of very large turbulence eddies. However, redistribution of the spectral energy is noted for all components above 0.005 m^{-1} , which is captured by the model very well. One of the important findings of this study is that for the u and w components the beam interference phenomenon will be observed at the heights in the mean wind direction at which the distance between the beams on the azimuth circle is equal to some odd multiple of the separation distance $(n-1)\Delta x$, $n\Delta x$ and $(n+1)\Delta x$; this is because of the assumption of Taylor's hypothesis. We observe the influence of this beam interference phenomenon at 100 m for the u and w components at approximately $2\Delta x$, $3\Delta x$, and $4\Delta x$.

For the v component, we observe an offset in the spectral energy at very low frequencies compared with those measured by the sonics. One of the reasons for this offset is the large contribution of $\Phi_{22}(\boldsymbol{k})$ as $\boldsymbol{k} \to 0$. Such an offset is also observed in our model, but

to a greater degree. We have speculated an explanation based on the difference in the shape of the modeled and the true two-dimensional spectrum $E_v(k_1, k_2)$. Due to lack of measurements of $E_v(k_1, k_2)$, we cannot verify our explanation. Furthermore, there is a small contribution of $F_{23}(k_1)$ in nature, which is not taken into account in the spectral tensor model.

We theoretically explained the interaction of the spectral tensors that cause redistribution of the spectral energy, and thus measurement of turbulence spectra using pulsed wind lidars is clarified. This study is particularly relevant for further understanding of how a pulsed wind lidar measures turbulent gusts. Given the complications displayed in this study, it might be advantageous to abandon the VAD technique for spectral analysis of lidar data, and instead analyze time series of individual beams. This approach is currently being pursued at Risø DTU, Denmark.

Acknowledgments. This study is part of a PhD project at Delft University of Technology. The experimental results are all based on data collected at the Høvsøre Test Station under the auspices of Anders Ramsing Vestergaard and Bjarne Sønderskov. This paper has been prepared using resources provided by the European Commission's FP7 SafeWind Project, Grant Agreement no. 213740, and by the Center for Computational Wind Turbine Aerodynamics and Atmospheric Turbulence funded by the Danish Council for Strategic Research grant no. 09-067216. Finally, the authors would like to thank Dr. Mike Courtney for useful comments and also checking the manuscript for English language errors.

References

Canadillas, B., A. Bégué, and T. Neumann (2010), Comparison of turbulence spectra derived from LiDAR and sonic measurements at the offshore platform FINO1, in *DEWEK 2010,* 10^{th} *German Wind Energy Conference.*

Courtney, M., R. Wagner, and P. Lindelow (2008), Testing and comparison of lidars for profile and turbulence measurements in wind energy, in 14^{th} *International Symposium for the Advancement of Boudary Layer Remote Sensing*, *IOP Conference Series Earth and Environmental Science*, vol. 1, edited by J. Mann et al., p. 012021, IOP Publishing LTD., doi:10.1088/1755-1315/1/1/012021.

Davenport, A. G. (1964), Note on the distribution of the largest value of a random function with application to gust loading, *ICE Proceedings*, *28*(2), 187–196, doi:10.1680/iicep.1964.10112.

Dors, I., J. P. McHugh, G. Y. Jumper, and J. Roadcap (2011), Velocity spectra and turbulence using direct detection lidar and comparison with thermosonde measurements, *Journal of Geophysical Research*, *116*, D01,102, 1–12, doi:10.1029/2010JD014606.

Drobinski, P., A. M. Dabas, and P. H. Flamant (2000), Remote measurement of turbulent wind spectra by heterodyne Doppler lidar technique, *Journal of Applied Meteorology*, *39*, 2434–2451, doi:10.1175/1520-0450(2000)039<2434:RMOTWS>2.0.CO;2.

Frehlich, R., S. M. Hannon, and S. W. Henderson (1998), Coherent doppler lidar measurements on wind field statistics, *Boundary-Layer Meteorology*, *86*(2), 233–256, doi:10.1023/A:1000676021745.

Genz, A. C., and A. A. Malik (1980), Remarks on algorithm 006: An Adaptive Algorithm for Numerical Integration over an N-dimensional Rectangular Region, *Journal of Com-*

putational and Applied Mathematics, *6*(4), 295–302, doi:10.1016/0771-050X(80)90039-X.

Gryning, S.-E., E. Batchvarova, B. Brümmer, H. Jørgensen, and S. Larsen (2007), On the extension of the wind profile over homogeneous terrain beyond the surface layer, *Boundary-Layer Meteorology*, *124*(2), 251–268, doi:10.1007/s10546-007-9166-9.

Hardesty, R. M., J. A. Korrell, and F. F. Hall (1982), Lidar measurement of wind velocity turbulence spectra encountered by a rotating turbine blade, *Technical Report DOE/RL/10236-81/1*, National Oceanic and Atmospheric Administration, Boulder, CO (USA).

IEC (2005), IEC 61400-1. Wind turbines – Part 1: Design Requirements.

Kaimal, J. C., and J. J. Finnigan (1994), *Atmospheric Boundary Layer Flows*, chap. Acquisition and processing of atmospheric boundary layer data, pp. 255–257, Oxford University Press, New York.

Kaimal, J. C., J. C. Wyngaard, Y. Izumi, and O. R. Coté (1972), Spectral characteristics of surface-layer turbulence, *Quarterly Journal of the Royal Meteorological Society*, *98*(417), 563–589, doi:10.1002/qj.49709841707.

Kaimal, J. C., J. C. Wyngaard, D. A. Haugen, O. R. Cote, Y. Izumi, S. J. Caughey, and C. J. Readings (1976), Turbulence structure in the convective boundary layer, *Journal of Atmospheric Sciences*, *33*(11), 2152–2169, doi:10.1175/1520-0469(1976)033<2152:TSITCB>2.0.CO;2.

Kristensen, L., D. H. Lenschow, P. Kirkegaard, and M. Courtney (1989), The spectral velocity tensor for homogeneous boundary-layer turbulence, *Boundary-Layer Meteorology*, *47*(1–4), 149–193, doi:10.1007/BF00122327.

Kristensen, L., M. Casanova, M. S. Courtney, and I. Troen (1991), In search of a gust definition, *Boundary-Layer Meteorology*, *55*(1–2), 91–107, doi:10.1007/BF00119328.

Kunkel, K. E., E. W. Eloranta, and J. A. Weinman (1980), Remote determination of winds, turbulence spectra and energy dissipation rates in the boundary layer from lidar measurements, *Journal of Atmospheric Sciences*, *37*(5), 978–985, doi:10.1175/1520-0469(1980)037<0978:RDOWTS>2.0.CO;2.

Lindelöw, P. (2007), Fibre based coherent lidars for remote wind sensing, PhD thesis, Technical University Denmark.

Lindelöw-Marsden, P. (2009), UpWind D1. Uncertainties in wind assessment with LIDAR, *Tech. Rep. Risø-R-1681(EN)*, Risø DTU.

Lothon, M., D. H. Lenschow, and S. D. Mayor (2009), Doppler lidar measurements of vertical velocity spectra in the convective planetary boundary layer, *Boundary-Layer Meteorology*, *132*(2), 205–226, doi:10.1007/s10546-009-9398-y.

Mann, J. (1994), The spatial structure of neutral atmospheric surface-layer turbulence, *Journal of Fluid Mechanics*, *273*, 141–168, doi:10.1017/S0022112094001886.

Mann, J., J. Cariou, M. Courtney, R. Parmentier, T. Mikkelsen, R. Wagner, P. Lindelow, M. Sjöholm, and K. Enevoldsen (2009), Comparison of 3D turbulence measurements using three staring wind lidars and a sonic anemometer, *Meteorologische Zeitschrift*, *18*(2, Sp. Iss. SI), 135–140, doi:10.1127/0941-2948/2009/0370.

Mayor, S. D., D. H. Lenschow, R. L. Schwiesow, J. Mann, C. L. Frush, and M. K. Simon (1997), Validation of NCAR 10.6-μm CO_2 Doppler lidar radial velocity measurements and comparison with a 915-MHz profiler, *Journal of Atmospheric and Oceanic Technology*, *14*(5), 1110–1126, doi:10.1175/1520-0426(1997)014<1110:VONMCD>2.0.CO;2.

Peña, A., C. B. Hasager, S.-E. Gryning, M. Courtney, I. Antoniou, and T. Mikkelsen (2009), Offshore wind profiling using light detection and ranging measurements, *Wind Energy*, *12*(2), 105–124, doi:10.1002/we.283.

Rice, S. O. (1944), Mathematical analysis of random noise, *Bell System Tech. J.*, *23*(3), 282–332.

Rice, S. O. (1945), Mathematical analysis of random noise, *Bell System Tech. J.*, *24*(1), 46–156.

Sathe, A., J. Mann, J. Gottschall, and M. S. Courtney (2011), Can wind lidars measure turbulence?, *Journal of Atmospheric and Oceanic Technology*, *28*(7), 853–868, doi:10.1175/JTECH-D-10-05004.1.

Sjöholm, M., T. Mikkelsen, J. Mann, K. Enevoldsen, and M. Courtney (2009), Spatial averaging-effects on turbulence measured by a continuous-wave coherent lidar, *Meteorologische Zeitschrift*, *18*(3, Sp. Iss. SI), 281–287, doi:10.1127/0941-2948/2009/0379.

Wyngaard, J. C. (2010), *Turbulence in the Atmosphere*, Cambridge University Press, New York.

Table 1: *Mann* [1994] model parameters to estimate $\Phi_{ij}(\boldsymbol{k})$

Height (m)	$\alpha\epsilon^{2/3}$	L (m)	Γ
60	0.051	46.226	3.158
100	0.037	60.867	2.896

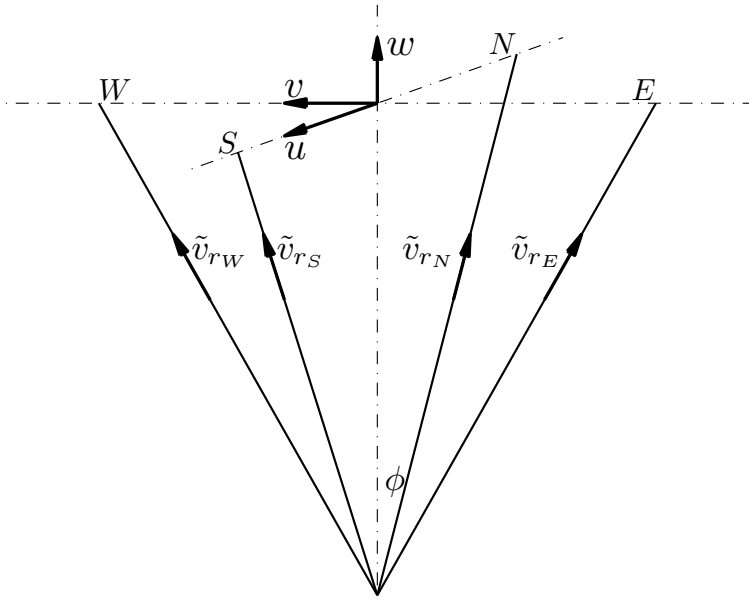

Figure 1: Schematic of the velocity Azimuth display scanning for the WindCube

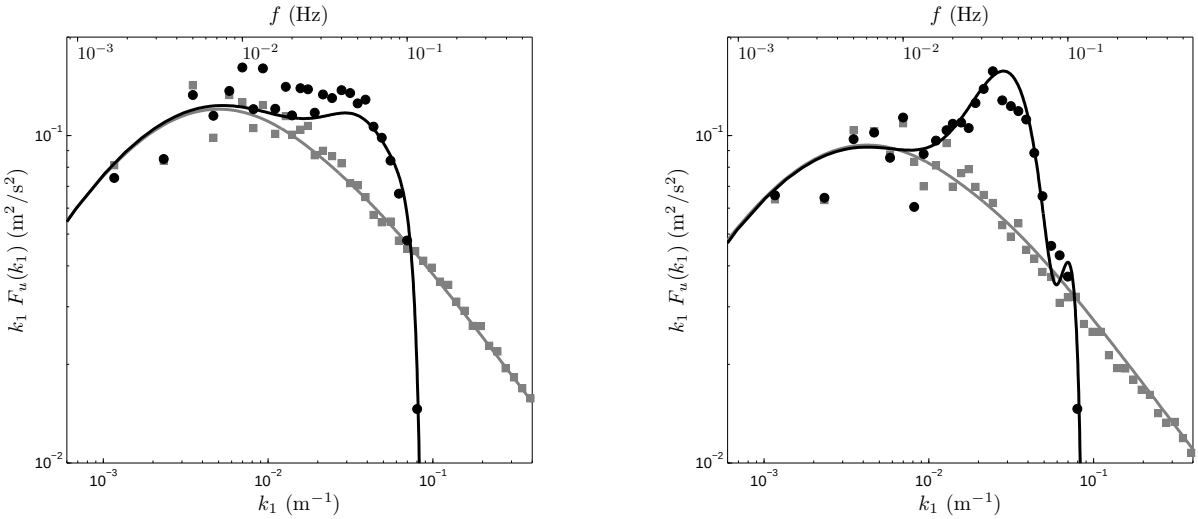

Figure 2: Comparison of the modeled and measured u spectrum at 60 m (left) and 100 m (right). The markers indicate measurements and the continuous line indicates the model. The black and gray markers denote WindCube spectrum and sonic spectrum, respectively.

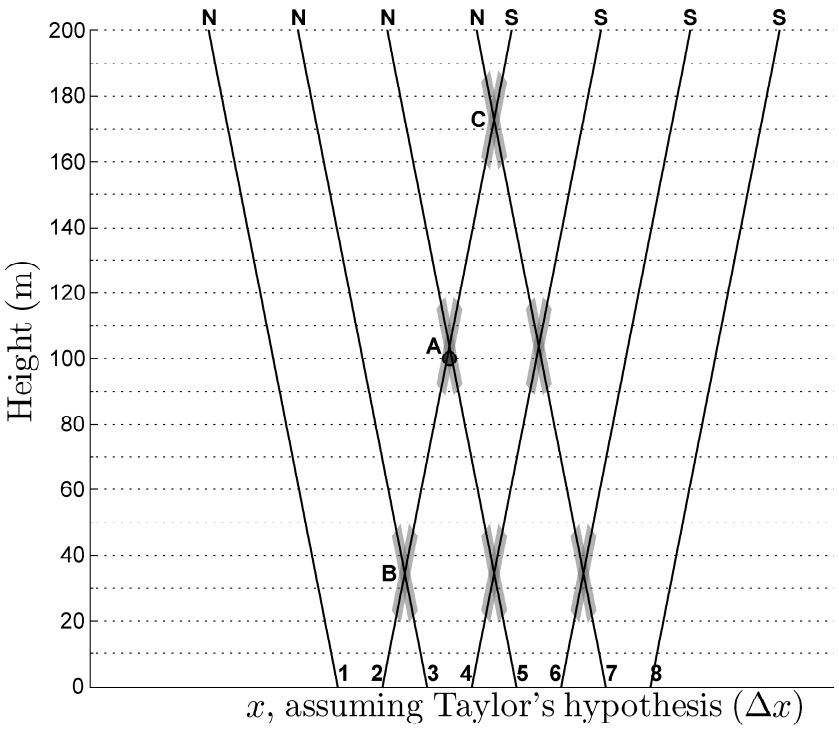

Figure 3: Schematic of the intersection of the North and South Beams. The shaded portion indicates the measurement volume. The black marker indicates a height of 100 m

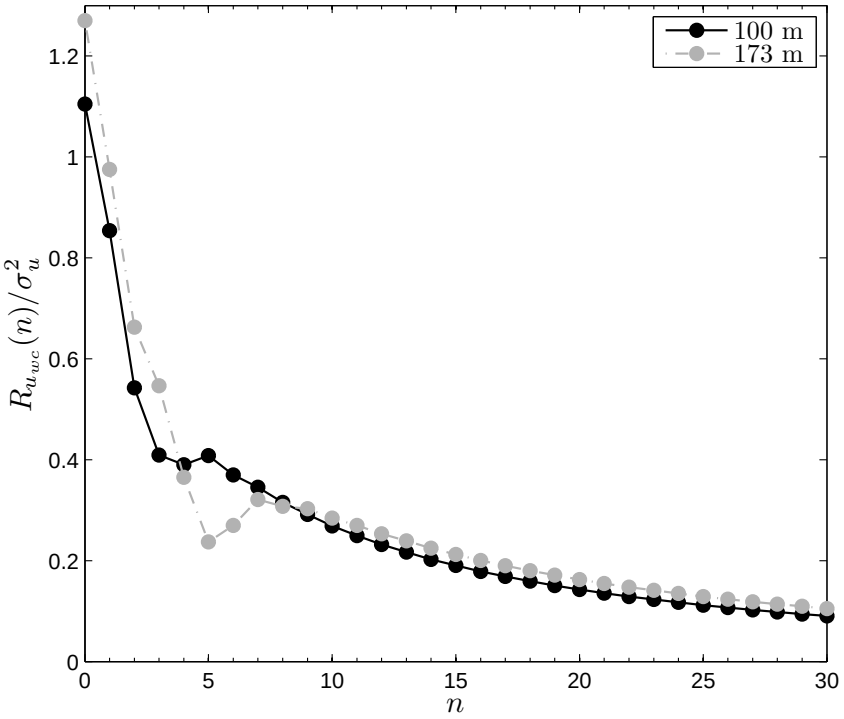

Figure 4: Comparison of $R_{u_{wc}}(n)/\sigma_u^2$ at different heights

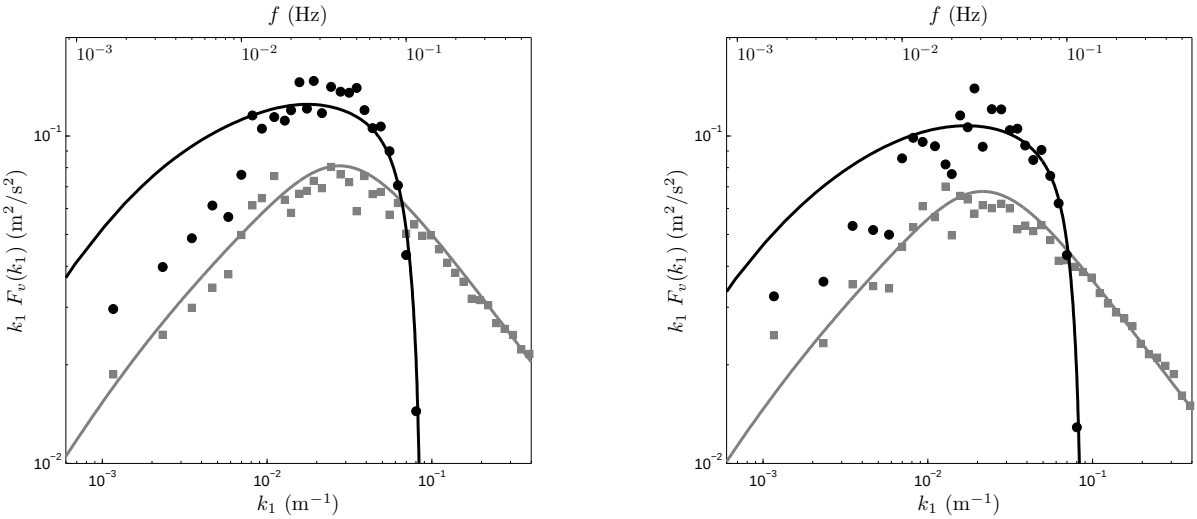

Figure 5: Comparison of the modeled and measured v spectrum at 60 m (left) and 100 m (right). The meaning of the symbols and colors correspond to those in Fig. 2

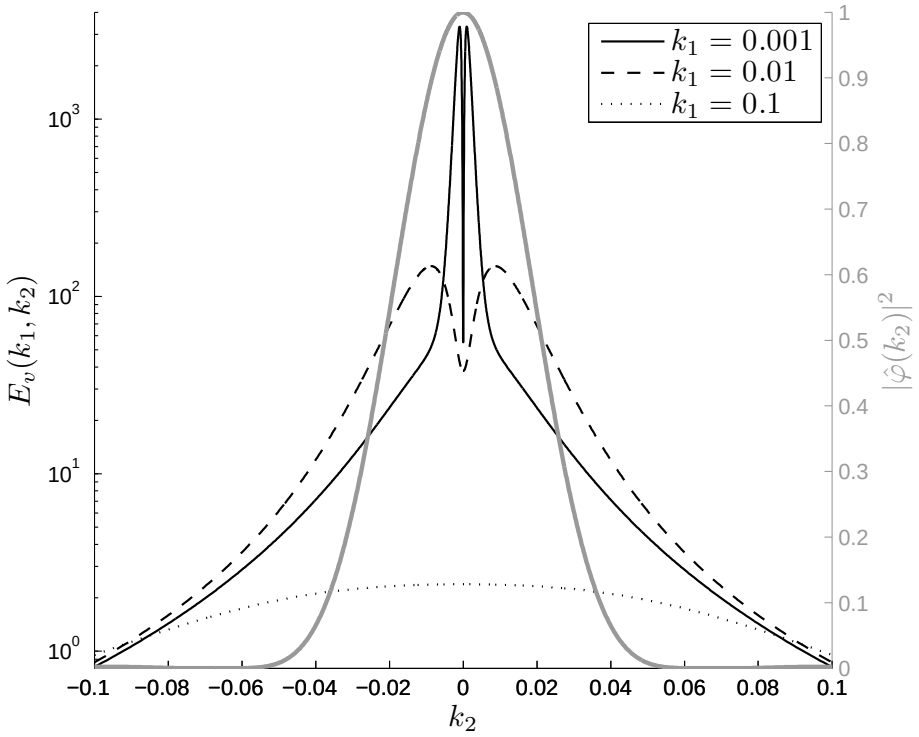

Figure 6: Two-Dimensional energy spectrum of the v component. The weighting function $|\hat{\varphi}(k_2)|^2$ is plotted on the right y-axis

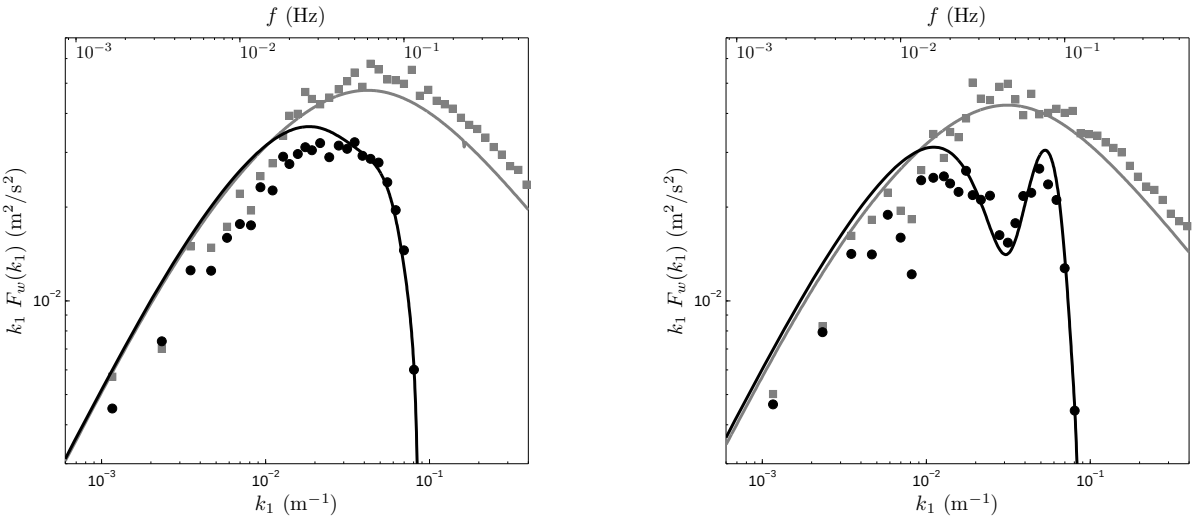

Figure 7: Comparison of the modeled and measured w spectrum at 60 m (left) and 100 m (right). The meaning of the symbols and colors correspond to those in Fig. 2